Geophysical Journal International

Geophys. J. Int. (2017) **209,** 234–249
Advance Access publication 2017 January 30
GJI Seismology

doi: 10.1093/gji/ggx013

The excitation of tsunamis by deep earthquakes

Emile A. Okal

Department of Earth and Planetary Sciences, Northwestern University, Evanston, IL 60208, USA. E-mail: emile@earth.northwestern.edu

Accepted 2017 January 13. Received 2016 September 22; in original form 2016 June 15

SUMMARY

Motivated by the detection of a millimetric tsunami following the deep earthquake of 2013 May 24 in the Sea of Okhotsk (depth 603 km; record moment $M_0 = 3.95 \times 10^{28}$ dyn cm), we present a number of theoretical studies of the influence of source depth, z_s, on the excitation of tsunamis by dislocation sources. In the framework of the static deformation of an elastic half-space, we show that the energy available for tsunami excitation by a seismic source whose depth is significantly greater than source dimensions is expected to vary as M_0^2/z_s^2, in contrast to the classical scaling as $M_0^{4/3}$ for shallow sources. This is verified by numerical simulations based on the MOST algorithm, which also confirm the interpretation of the millimetric signals observed on DART sensors during the 2013 event. The normal-mode formalism, which considers tsunamis as a special branch of the spheroidal oscillations of the Earth in the presence of a water layer at its surface, also predicts an M_0^2/z_s^2 scaling for point source double-couples, and confirms millimetric amplitudes in the geometry of the DART buoys having recorded the 2013 Okhotsk tsunami. A general investigation of potential tsunami excitation as a function of depth for realistic intermediate and deep sources suggests the admittedly remote possibility of damaging events if deep earthquakes even greater than the 2013 event could occur at the bottom of Wadati-Benioff zones.

Key words: Tsunamis; Theoretical seismology; Pacific Ocean.

1 INTRODUCTION AND BACKGROUND

The title of this paper is in itself a paradox, since common wisdom has long held that deep earthquakes at the bottom of subduction zones do not generate observable tsunamis. However, this paradigm was proven wrong during the Sea of Okhotsk earthquake of 2013 May 24, which generated a tsunami detectable on at least two stations of the DART network. In this context, the present study serves multiple purposes. First, we analyse those records and justify their interpretation as a tsunami generated by the deep earthquake. In addition, we conduct a theoretical study of the excitation of tsunamis by earthquake sources as a function of depth, including the very deepest ones, down to 690 km. We confirm our analytical results using numerical simulations.

The 2013 Sea of Okhotsk earthquake (54.6°N, 153.77°E; origin time 05:44:49 GMT) featured the remarkable combination of having the largest seismic moment ever measured for a deep shock (hypocentral depth $z_s = 603$ km; moment $M_0 = 3.95 \times 10^{28}$ dyn cm) and of occurring at a subduction zone offering a marginal sea where a tsunami could be generated. The runner-up events (Bolivia, 1994 June 9; $M_0 = 2.6 \times 10^{28}$ dyn cm; Colombia, 1970 July 31; $M_0 = 1.8 \times 10^{28}$ dyn cm) took place under continental masses, and thus resulted in a significantly reduced deformation of the ocean floor (roughly, as derived below, by a factor of 2 for a 45° dip of the slab).

Following the Sea of Okhotsk earthquake, a small tsunami signal was recorded by two DART sensors (Okal 2014; Williamson *et al*. 2015; Zaitsev *et al*. 2016). We recall that these ocean observatories consist of a pressure microsensor deployed on the seafloor, communicating acoustically with a buoy floating on the surface, where the signal is relayed by satellite to a distant receiving laboratory (Bernard *et al*. 2001). In the particular case of the 2013 Sea of Okhotsk earthquake, Fig. 1 shows records at DART stations 21402 and 21419, located at (46.49°N, 158.34°E) and (44.45°N, 155.74°E), respectively, in the Pacific Basin off the Northern Kuril Island chain. The tsunami can be identified as the faint oscillations occurring around 08:00 GMT (arrows on Figs 1a and b), featuring a peak-to-peak amplitude of a few mm, the dominant long-period oscillation being the tide. This interpretation is confirmed by filtering (Fig. 1c) and by a spectrogram analysis, shown on Fig. 2, which documents a build-up of energy in the 2 mHz frequency range around that time. Estimating the expected arrival time of the tsunami is made difficult by the fact that it originates in the Sea of Okhotsk, in waters only 1500 m deep on the average, and must enter the deep Pacific Ocean basin through a series of narrow straits between the Kuril Islands. In addition, the 2013 earthquake features a décollement focal mechanism ($\phi = 189°$; $\delta = 11°$; $\lambda = -93°$), resulting in a dipolar distribution of seafloor displacement, the great depth of the source leading to a long lever of ∼550 km for the dipole. In this context, we define expected times of arrival (ETA) for the

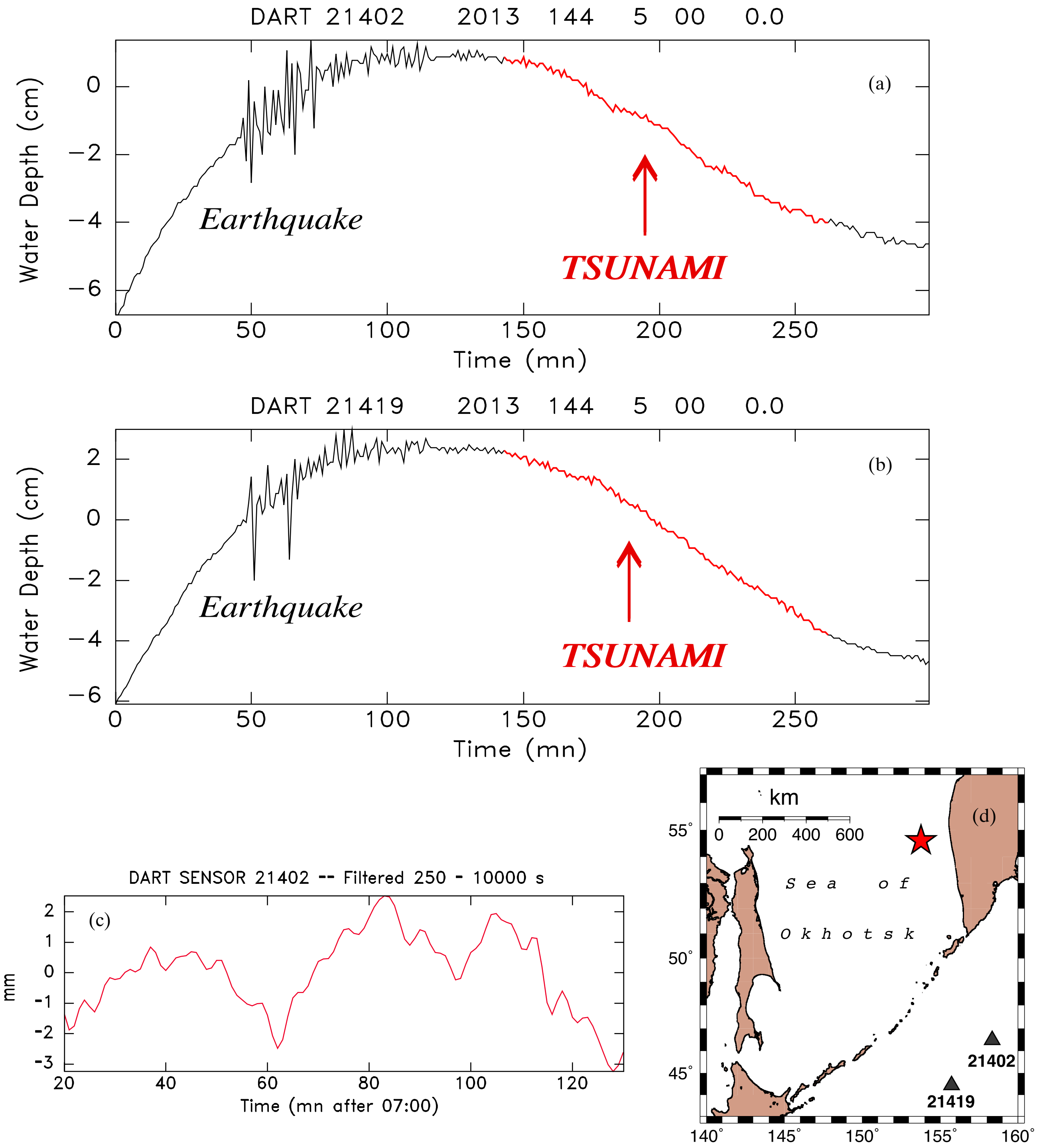

Figure 1. (a,b) Time-series recorded by DART sensors 21402 and 21419, expressed in equivalent water depth. The zero level of ordinates is arbitrary. The records start at 05:00 GMT on Day 144 (2013 May 24) and run for 6 hr. The large signals at left are the earthquake waves; the signals attributable to the tsunami are highlighted in red. (c) Excerpt of the 21402 record, starting at 07:20 GMT, and filtered between 0.1 and 4 mHz. Note the millimetric peak-to-peak amplitude and the dominant period of about 40 min, (d): Location map showing the epicentre (star) and the position of the two DART sensors.

tsunami by considering two point sources (one for each polarity of the dipole) located at the edge of the marine domain of 1-cm uplift or subsidence (based on a static deformation estimate using Mansinha & Smylie's (1971) algorithm; see Section 2), and a probable path through the Kuril chain, as shown on Fig. 3. The resulting ETAs are shown as a function of frequency on the spectrograms, and confirm that the observed energy build-up can be attributed to the tsunami.

The main signal in the time-series presented on Fig. 1, occurring between 05:50 and 06:15 GMT, can be interpreted as the recording, by the pressure sensor, of the body and surface seismic waves generated by the earthquake, both of which create a pressure perturbation in an oceanic column overlying a half-space. Unfortunately, the operational protocol of the DART sensor restricts the sampling of the time-series to 15 min in 'sleep mode', upgraded to 1 min when

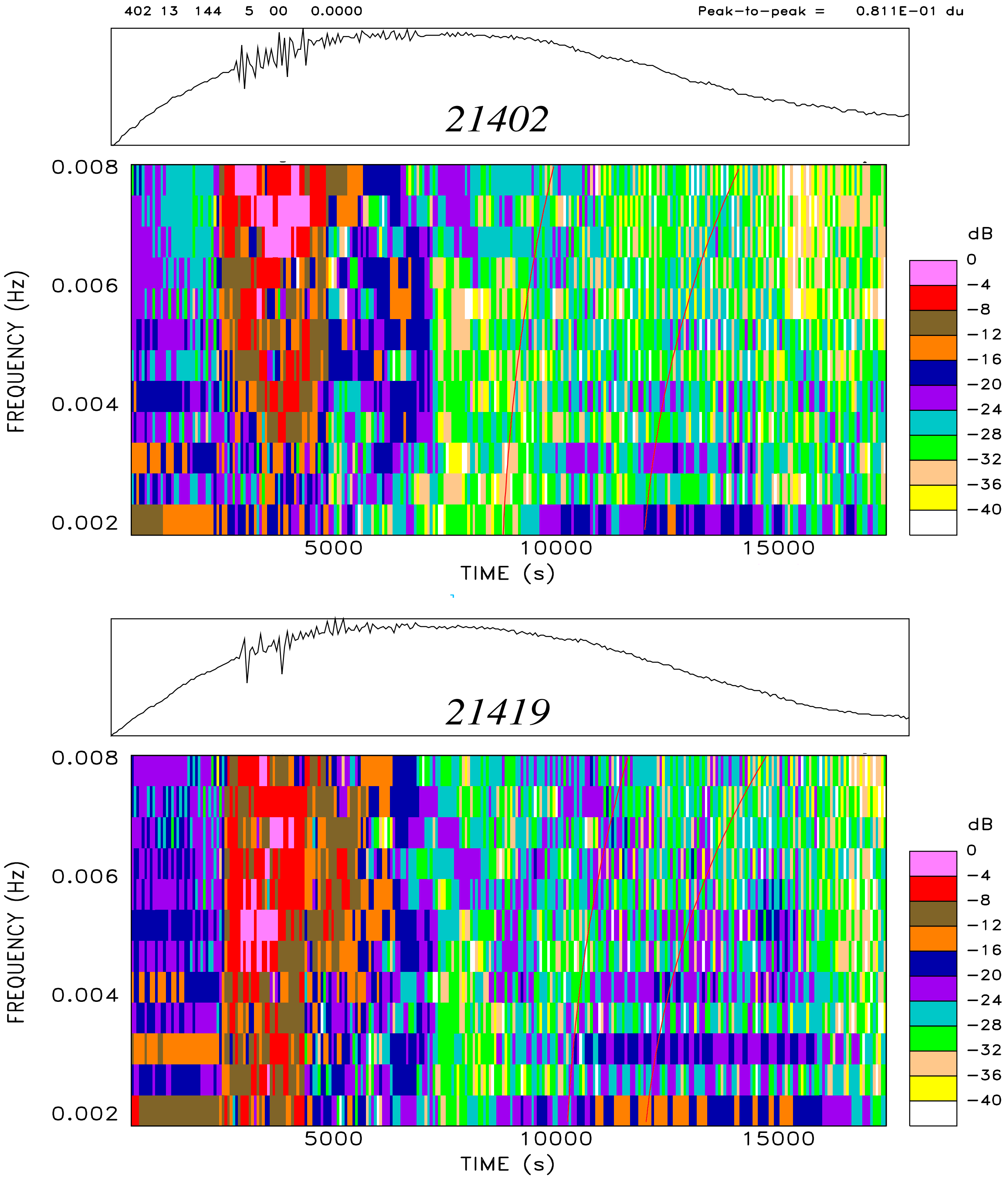

Figure 2. Time–frequency spectrograms of the DART records 21402 (top) and 21419 (bottom). The records are Fourier-analysed through a window sliding in time, and the spectral energy at each time–frequency pixel is colour-coded according to the logarithmic scale at right. The tsunami is identified as the build-up of very low frequency energy (2 mHz) about 10 000 s into the records (07:45 GMT) in an otherwise very quiet window. The estimated times of dispersed arrival from the two poles of ocean floor deformation are shown as the red lines, which agree well with the onset of the low-frequency energy. The massive energy earlier in the records corresponds to the seismic waves from the earthquake.

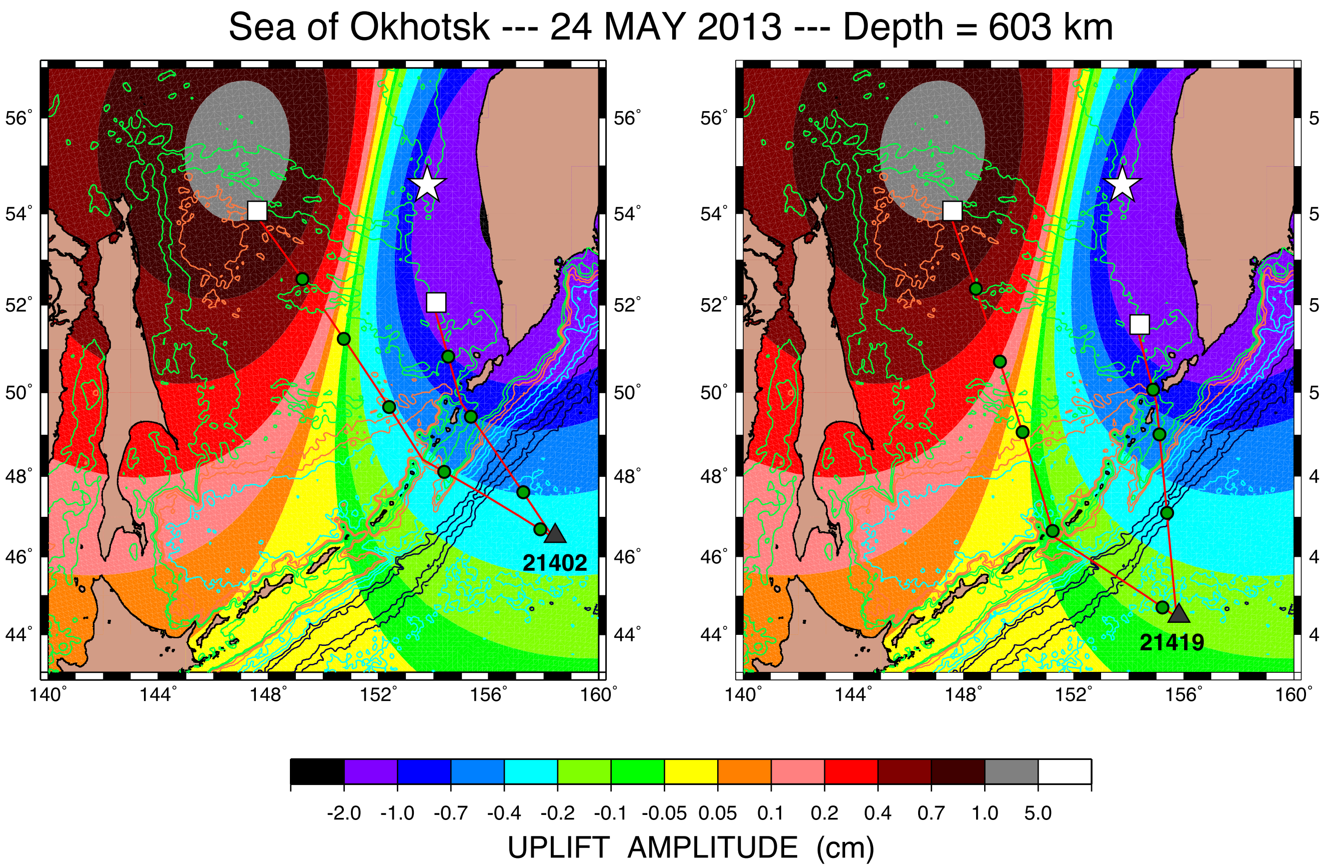

Figure 3. The static displacement at the ocean floor, computed in the formalism of Mansinha & Smylie (1971), is used to interpret the probable paths of the observed tsunami to DART sensors 21402 (left) and 21419 (right). The white star represents the epicentre, and the squares the elements of the poles (of subsidence and uplift, respectively) used to compute the times of arrival plotted on the spectrograms (Fig. 2), estimated along the probable paths through the Kuril Islands straits. Along the paths, the green dots represent 30-min increments in travel-time.

a disturbance (in practice the passage of a seismic surface wave) is detected (e.g. Mofjeld 2008). This time sampling is adequate for studying tsunamis with typical periods of 15 min or longer, but is too coarse for rigorous quantitative processing of seismic waves. Nevertheless, it is possible to verify this interpretation of the main DART signals, as detailed in the Appendix.

Unfortunately, no signals could be definitely identified at other DART stations, due in part to the sampling protocol, which prevented most of them from switching to 1-mn sampling. Those which did, for example, Station 21415 whose record is described by Zaitsev *et al.* (2016), recorded only the mantle waves (arriving around 06:00 GMT), but failed to detect the tsunami beyond the spectrogram noise level. Similarly, records at land-based tidal gauge stations in Sakhalin and the Kuril Islands were mentioned and in one instance (Kuril'sk, Iturup Island) simulated by Zaitsev *et al.* (2016). These records are digitized with a precision of only 1 cm, and unfortunately, their spectrograms do not convincingly feature energy rising above background noise levels.

2 THE STATIC APPROACH (MANSINHA AND SMYLIE, KAJIURA)

2.1 Theoretical background

We recall that the traditional method of simulation of tsunamis generated by earthquakes consists of burying a properly oriented fault surface Σ in an infinite half-space, and of computing the static field of vertical deformation $h\,(x, y)$ at the surface of the half-space, using the analytical solutions derived by Mansinha & Smylie (1971) or Okada (1985). It is then assumed that this deformation field is transferred instantaneously to the surface of the ocean, where it is taken as the initial condition $\eta\ (x,\ y;\ t\ =\ 0_+)$ for the numerical solution of the hydrodynamic equations governing the propagation of the tsunami.

In this traditional approach, and for shallow earthquakes, the energy of a tsunami is computed as the difference between the work spent against the pressure forces during the deformation of the bottom of the ocean, and the gain in gravitational energy resulting from the transfer of the displaced masses of water from the seafloor to their eventual equilibrium at the surface, the latter assumed unchanged for $t \rightarrow \infty$ on account of the size of the ocean basin. This difference arises from the fact that the transfer of water from bottom to surface is taken as instantaneous, and thus thermodynamically irreversible. By contrast, for a very slow, reversible, deformation of the ocean bottom (such as takes place during an interseismic cycle), the displaced water is transferred only to the (flat) ocean surface, the pressure at the bottom is constantly readjusted, and the work opposing it exactly equals the required change of gravitational energy, without any waste; no tsunami is generated. In this respect, the critical condition for the generation of a tsunami is that the rise time of the seismic source (typically a matter of seconds for regular earthquakes, but days for 'slow slip' (Schwartz & Rokosky 2007) and decades for interseismic creep) should be much shorter than the period of the waves being generated (typically tens of minutes).

Assuming the simple model of an element of ocean bottom of cross-section S displaced vertically in an amount h, the work against the pressure forces takes the form

$$W = \rho_{\mathrm{w}} g H S h \tag{1}$$

where H is the thickness of the ocean column, ρ_{w} the density of water, and g the acceleration of gravity. The gain in potential energy is obtained by considering the motion of the centre of mass of the displaced water from a depth $H - h/2$ to the surface (depth zero):

$$E^{\mathrm{Pot.}} = \rho_{\mathrm{w}} S h g \,(H - h/2)\,; \tag{2}$$

hence the energy of the tsunami is

$$E^{\mathrm{Tsu.}} = W - E^{\mathrm{Pot.}} = \frac{1}{2} \rho_{\mathrm{w}} g S h^2 \tag{3}$$

Note that (3) is also the difference in potential energy of the displaced water of mass ($\rho_{\mathrm{w}}\ S\ h$) between its location as the unstable hump (of average height $h/2$) created on the surface at $t = 0_+$ and its final equilibrium distribution on the infinite, undisturbed surface of the ocean for $t \to \infty$. In this context, it is clear that (3) does not depend on the thickness H of the ocean column. Note further that, as expected from the Second Law of thermodynamics, $E^{\mathrm{Tsu.}}$ is always positive, regardless of the sign of h.

For deformations due to a shallow earthquake, the displacement h can be taken as directly proportional to the slip Δu on the fault, through a non-dimensional trigonometric coefficient, and the surface S as proportional to the area of rupture Σ on the fault. Under seismic source scaling laws, Δu will scale with seismic moment as $M_0^{1/3}$, and Σ as $M_0^{2/3}$ (Kanamori & Anderson 1975; Geller 1976), resulting in $E^{\mathrm{Tsu.}}$ scaling as $M_0^{4/3}$. This result, first given by Aida (1977) and later Kajiura (1981; eq. (12) p. 421), was also verified by Okal (2003) using normal-mode theory.

In the case of a source located at significant depth z_{s} into the solid Earth, the simple expression (3) must be replaced by

$$E^{\mathrm{Tsu.}} = W - E^{\mathrm{Pot.}} = \frac{1}{2} \rho_{\mathrm{w}} g \int\!\!\int h^2(x, y)\, \mathrm{d}S_{x,y} \tag{4}$$

where the integral should, conceptually, be extended over the entire plane constituting the bottom of the ocean. In the limit of a source of small dimensions compared to the depth z_{s} of the source, the displacement h of the bottom of the ocean is computed from the static (near field) component of the classical Green's function of a point-source double-couple, as given, for example, by Aki & Richards (1980; eq. (4.29) p. 79). The fundamental result is that the displacement h at a point (x, y) on the ocean floor is proportional to M_0, but varies like the inverse squared of its distance to the source:

$$h(x, y) = \frac{\Phi}{\mu} \times \frac{M_0}{(x^2 + y^2) + z_s^2} \tag{5}$$

where μ is the rigidity of the solid half-space, and Φ a non-dimensional factor, which combines the trigonometric functions expressing the orientation of the receiving point with respect to the focal mechanism, and the 'response' of the surface, that is, the local contributions of reflection and conversion (in the sense of $P \longleftrightarrow S$) at the free surface (Okal 1992); it also depends, in principle, on the Poisson ratio of the medium, which can be taken as 1/4 following Mansinha & Smylie (1971). Substituting (5) into (4), we predict that the energy of a tsunami generated by an earthquake of large hypocentral depth z_{s} will vary as

$$\begin{aligned} E^{\mathrm{Tsu.}} &= \frac{1}{2} \frac{\rho_{\mathrm{w}} g}{\mu^2} M_0^2 \int_{-\infty}^{\infty} \int_{-\infty}^{\infty} \frac{\Phi^2(x, y)}{\left[r^2 + z_{\mathrm{s}}^2\right]^2} \mathrm{d}x\ \mathrm{d}y \\ &= \frac{1}{2} \frac{\rho_{\mathrm{w}} g}{\mu^2} M_0^2 \overline{\Phi^2} \int_{-0}^{\infty} \frac{2\pi\, r\, \mathrm{d}r}{\left[r^2 + z_{\mathrm{s}}^2\right]^2} = \frac{\pi}{2} \frac{\rho_{\mathrm{w}} g}{\mu^2}\, \overline{\Phi^2}\, \frac{M_0^2}{z_{\mathrm{s}}^2} \end{aligned} \tag{6}$$

where $\overline{\Phi^2}$ is an appropriate average of Φ^2, which appears as a counterpart to the coefficient F [hereafter $F^{\mathrm{Kaj.}}$], as introduced by Kajiura (1981; eq. (10)), and should remain a fraction of unity. This formula will remain valid only for source dimensions small with respect to z_{s}. We note that Okada (1995) also proposed a formula of the type (6) (his eq. (5)), but only on empirical grounds, as an average of a large number of simulations performed for a relatively small seismic source ($M_0 = 10^{25}$ dyn cm), and depths not exceeding 30 km.

We thus come to the conclusion that the energy of a tsunami should scale like $M_0^{4/3}$ at shallow depths, but grow like M_0^2 for very deep earthquakes. This result may seem paradoxical, but can be explained very simply in the framework of interferences caused by source finiteness. Assume first that the hypocentral depth z_{s} is very large with respect to source dimensions; then for any given point on the ocean floor, the contributions to ground motion of the various elements of the fault are essentially identical, and their interference is constructive; as a result h grows linearly with moment and $E^{\mathrm{Tsu.}}$ with M_0^2. If, on the other hand, the dimensions of the source are comparable to, or even greater than, z_{s}, then destructive interference will result in values of h growing slower than M_0, and of the energy $E^{\mathrm{Tsu.}}$ growing slower than M_0^2. It is noteworthy that Ward (1980) originally argued for $E^{\mathrm{Tsu.}}$ proportional to M_0^2 by considering only point sources, but later revised his proposed power law to $M_0^{1.5}$ (but not to the more justifiable $M_0^{4/3}$), when considering source finiteness (Ward 1982).

2.2 Comparison with numerical simulations

In this section, we test the validity of eq. (6) on a data set of numerical applications of Mansinha & Smylie's (1971) analytical solution. We consider 17 hypocentral depths, varying from shallow (10 km) to deep (690 km), the latter being the depth of the deepest earthquakes (Okal & Bina 1998), and five levels of seismic moment, equally spaced geometrically from 10^{27} to 10^{29} dyn cm; for each of them, we use scaling laws (Kanamori & Anderson 1975; Geller 1976) to infer appropriate values of the faulting parameters (fault length L, width W, and seismic slip Δu). We then consider five different focal mechanisms: (i) pure strike-slip on a vertical fault ($\delta = 90°$; $\lambda = 0°$); (ii) pure dip-slip on a vertical fault ($\delta = 90°$; $\lambda = 90°$); (iii) pure thrust on a 45°-dipping fault ($\delta = 45°$; $\lambda = 90°$); (iv) pure thrust on a shallow-dipping fault (more representative of a mega-thrust earthquake at a subduction zone ($\delta = 15°$; $\lambda = 90°$)); and finally (v) a hybrid mechanism ($\delta = 45°$; $\lambda = 45°$).

For each of these 425 source models, we compute the vertical deformation at the surface using Mansinha & Smylie's (1971) analytical solution, on a square grid of 40401 points, the side of the square measuring 3000 km. The model of a flat homogeneous half-space is only a crude approximation to the real Earth, especially for the deepest sources, located more than 10 per cent of the Earth's radius into the Earth, through a medium in which the rigidity μ increases by a factor of 2 from top to bottom. For this reason, we use for each of the 17 source depths a value of μ averaged over the overlying mantle. In addition, we have verified in the case of the

2013 Sea of Okhotsk earthquake that a more elaborate computation using the STATIC-1D Code (Pollitz 1996) based on an expansion on the Earth's normal modes (albeit only for a point source double-couple) yields comparable results for the field of deformation at the Earth's surface (Pollitz, private communication, 2013).

We retain a data set consisting, for each source model, of the maximum and minimum values, $h_{\max}$ and $h_{\min}$ of h (x, y), over the grid, and of the energy $E^{\mathrm{Tsu.}}$ obtained by numerically computing the integral (4) on the grid.

We first examine the variation of $h_{\max}$ with depth. In the context of eq. (5), we give on Fig. 4 representative examples for constant moment and focal mechanism. As expected, the dependence on z_{s}^2 is verified only for depths large with respect to the fault dimensions, and hence the logarithmic plots on Fig. 4 exhibit increasing curvature with increasing M_0. This is expressed by a better fit of the power law between $h_{\max}$ and z_{s} for the smaller earthquakes (with slopes approaching -1.8) than for large ones (with poor fits and average slopes close to -1.2). These results are found to be largely independent of focal mechanism, the latter affecting principally the absolute values of $h_{\max}$, especially in the case of strike-slip events, which feature expectedly lower values of $h_{\max}$. They are also essentially unchanged when considering the *range* of vertical deformation, $(h_{\max} - h_{\min})$.

We similarly examine on Fig. 5 the variation of $h_{\max}$ with moment at constant source depth. Representative examples for shallow (*a*) and deep (*b*) sources document an increase in the slope of the power law between M_0 and $h_{\max}$. As expected, the slope approaches 1/3 for shallow sources, in a regime where $h_{\max}$ is directly proportional to the fault slip Δu, but it tends to 1 for deep sources, as expected from (5). Again, these results are largely insensitive to focal mechanism, and would be unchanged when considering the peak-to-peak deformation $(h_{\max} - h_{\min})$.

We next consider the case of the tsunami energy, as defined by (6). For each value of the depth z_{s}, we study the variation of E^{Tsu} with seismic moment M_0. Typical examples are presented on Fig. 6. Again, as in the case of $h_{\max}$, strike-slip mechanisms result in significantly lower energy values, on the average by a factor of 9. Their inclusion in the data set increases the scatter in individual values of $E^{\mathrm{Tsu.}}$ but does not change appreciably the regression slopes at constant depth. As documented on Fig. 6, the best-fitting slope defining the exponent of the power law between M_0 and $E^{\mathrm{Tsu.}}$ varies from ~1.4 at shallow depths, in satisfactory agreement with the value 4/3 predicted by Kajiura (1981) and Okal (2003), to 1.97 at 690 km, in excellent agreement with (6).

We also investigate the variation of $E^{\mathrm{Tsu.}}$ with depth for a given focal mechanism and moment. Representative examples are shown on Fig. 7. Once again, we find that smaller events, featuring reduced source dimensions, have predicted tsunami energies scaling as z_{s}^{-2}, while larger ones, whose source dimensions become comparable to z_{s} at shallow depths, show a weaker dependence on depth for shallow sources, and hence curvature in the $E^{\mathrm{Tsu.}}$ versus z_{s} logarithmic plots; we have verified that this behaviour applies to all focal mechanisms.

2.3 Hydrodynamic simulations

In this section, we carry out numerical hydrodynamic simulations using the MOST code (Titov & Synolakis 1998), with initial conditions derived from the static displacements computed in Section 2.2. We restrict ourselves to the 45°-thrust focal geometry and to three levels of moment: 10^{27}, 10^{28} and 10^{29} dyn cm. We consider a basin of homogeneous depth H on a spherical Earth, and use the values $H = 4$ km (typical average depth in the Pacific Ocean), $H = 2$ km (typical depth in the Sea of Okhotsk) and the admittedly unrealistic value $H = 6$ km, which allows a theoretical study of any possible influence of H on the variation of tsunami excitation with depth. We consider 16 centroid depths, ranging from 25 to 690 km, for a total of 144 simulations.

The MOST algorithm solves the full non-linear equations of hydrodynamics under the shallow-water approximation, by finite differences and through the method of alternate steps (Godunov 1959). MOST has been extensively validated through comparisons with laboratory and field data, per standard international protocols; full details can be found in Synolakis (2003) and Titov *et al.* (2016). The calculations are performed on a basin comparable in size to the Pacific Ocean. Time-series of sea-surface displacements $\eta_i(t)$ are stored at 284 virtual gauges (indexed i), distributed on semi-circular arcs located at distances of 30°, 60°, 90° and 120° from the epicentre. The duration of the time-series ranges from 7800 s for $H = 6$ km to 14 000 s for $H = 2$ km.

We seek to compute an energy flux at each of the gauges G_i in the following way: at any given time the density of kinetic energy due to the vertical motion of the surface is

$$E_z = \frac{1}{2}\rho_{\mathrm{w}}\dot{\eta}^2 \tag{7}$$

to which we must add the much larger term due to the horizontal motion

$$E_x = \frac{1}{2}\rho_{\mathrm{w}}\left(\eta\frac{C}{H}\right)^2 \tag{8}$$

where C is the velocity of propagation of the tsunami (undispersed under the shallow water approximation used in MOST). Over a time dt, there will be an energy flux per unit area of wave front

$$\mathrm{d}E = 2\,(E_z + E_x)\,C\,\mathrm{d}t, \tag{9}$$

the factor 2 accounting for the contribution of gravitational energy, equal to that of kinetic energy. The full energy of the tsunami will be the time integral of (9), itself integrated over the wave front. This can be decomposed into an azimuthal integral along the arc, and a depth integral over the ocean column of thickness H. The former can be discretized using the array of virtual gauges G_i, along the arc, and for the latter, E_x can be taken constant throughout the water column, but the average value of E_z will be 1/3 the value at the surface (7) since the vertical displacement will vary linearly with depth, vanishing at the bottom:

$$E^{\mathrm{Tsu.}} = 2\rho_{\mathrm{w}}C\,a\sin\theta\int_{-\pi/2}^{\pi/2}\mathrm{d}\phi\left(\frac{H}{3}\int_0^\infty\dot{\eta}^2\mathrm{d}t + \frac{C^2}{H}\int_0^\infty\eta^2\mathrm{d}t\right), \tag{10}$$

the factor 2 expressing the contribution of the full circular arc (from $-\pi$ to π), given the symmetry of the mechanism considered. Here a is the radius of the Earth, and θ the epicentral distance at the arc of gauges. We have verified numerically that, as expected under conservation of energy, the numerical estimates (10) are independent of the distance θ to the arc, so we simply retain those computed at $\theta = 30°$.

The logarithmic plots on Fig. 8 show the dependence of $E^{\mathrm{Tsu.}}$ on moment at constant depth (left) and on depth at constant moment (right). Regression slopes at constant depth vary from 1.63 at 25 km to 1.98 at 690 km, and at constant moment from -1.98 at 10^{27} dyn cm to -1.50 for 10^{29} dyn cm.

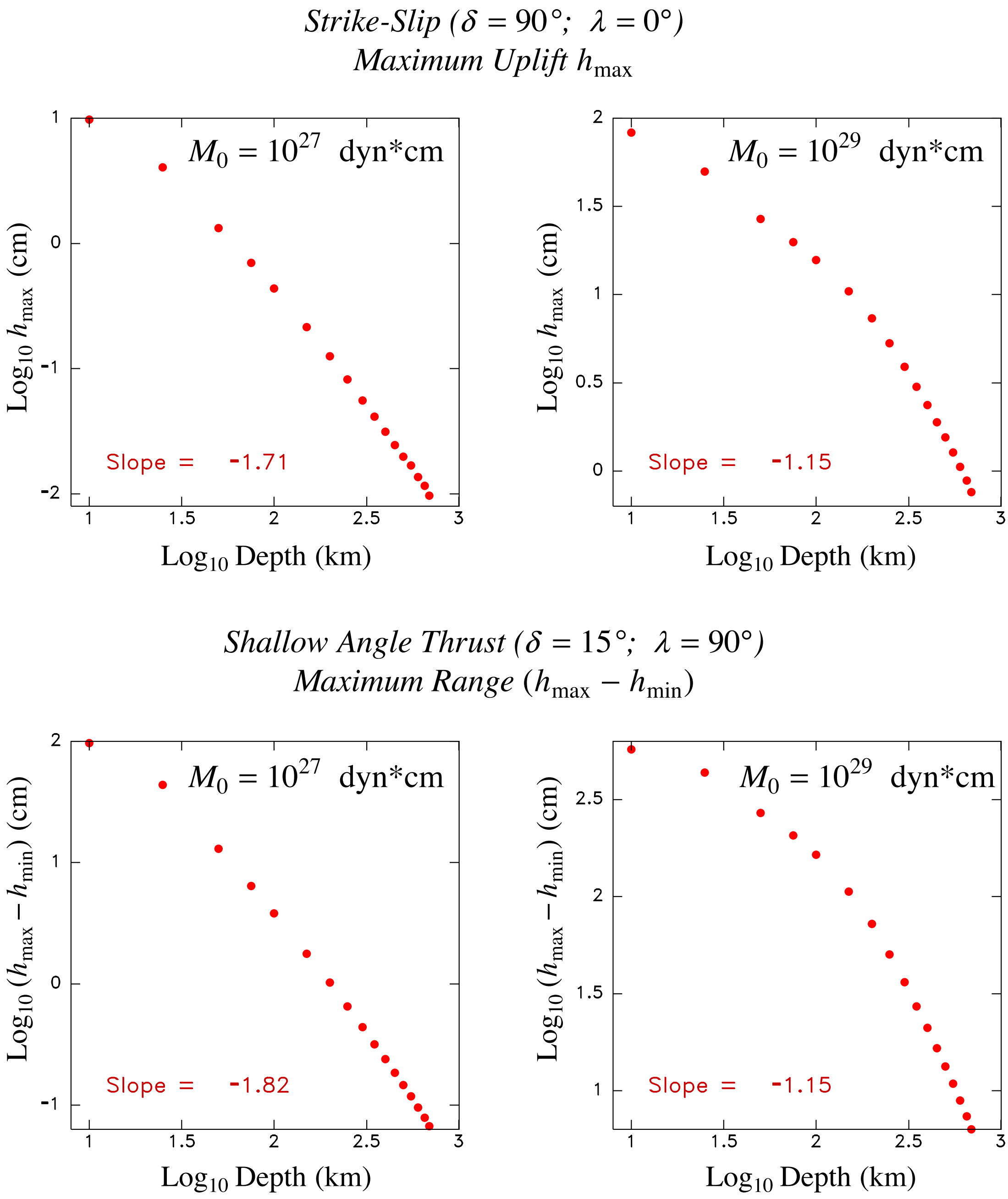

Strike-Slip ($\delta = 90°$; $\lambda = 0°$)
Maximum Uplift $h_{\max}$

Shallow Angle Thrust ($\delta = 15°$; $\lambda = 90°$)
Maximum Range ($h_{\max} - h_{\min}$)

Figure 4. Representative examples of the variation of static uplift with depth. Top: Parameter $h_{\max}$ for a strike-slip mechanism; bottom: range of vertical deformation ($h_{\max} - h_{\min}$) for a shallow-angle thrust mechanism. In each case, the frames compare a small source (left) to a large one (right). Note that the small source approaches the theoretical behaviour (5), but the large one, for which source dimension becomes comparable to source depth, exhibits curvature. The slopes of a linear logarithmic regression for the 17 depths considered are given for each frame.

Another method of analysis consists of assuming that $E^{\mathrm{Tsu.}}$ takes the form (6) and of computing a value of $\overline{\Phi^2}$. Such values are computed from the integrals (9) of the field of MOST simulations, and colour-coded on Fig. 9. In the domain where (6) applies (small and/or deep sources), we find $\overline{\Phi^2} \approx 0.02$, which corresponds to an average $\Phi \approx 0.14$, which has the right order of magnitude for a coefficient combining the effects of source radiation and surface response. Note however that $\overline{\Phi^2}$ cannot be directly compared to $F^{\mathrm{Kaj.}}$ which is derived under the significantly different model appropriate for shallow sources with dimensions comparable to, if not greater than, z_s.

2.4 MOST modelling of the 2013 deep Okhotsk tsunami

We conclude this section by presenting a MOST simulation of the 2013 tsunami at the locations of DART sensors 21402 and 21419. Our purpose is to justify the amplitudes observed on Fig. 1. The hydrodynamic simulation uses the exact bathymetry of the Sea of Okhotsk and Pacific Basin, including the coastlines of Kamchatka and the Kuril Islands, but the initial conditions are obtained from a simple application of Mansinha & Smylie's (1971) formalism for a homogeneous half-space, which neglects both the radial layering of the Earth structure between the source depth (603 km) and the surface, and the curvature of the Earth. Nevertheless, our results,

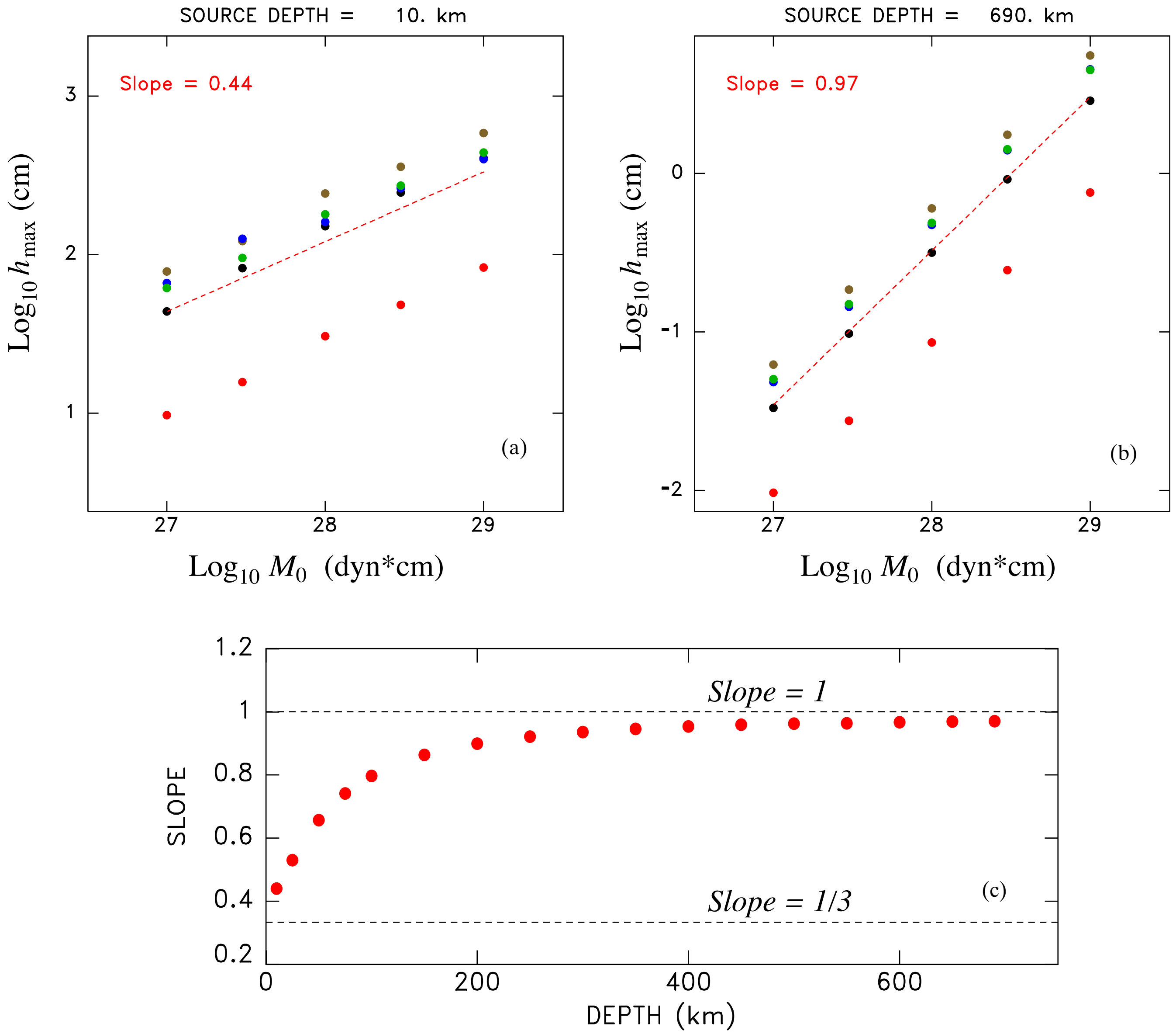

Figure 5. Top: representative examples of the variation of static uplift with moment at depths of 10 km (a) and 690 km (b). Individual solutions are colour-coded for each of the five focal geometries: Red: strike-slip mechanism; black: dip-Slip; brown: 45°-Thrust Fault; blue: shallow-angle thrust fault; green: hybrid mechanism. At each depth, a linear regression of the entire data set is shown as the dashed line, and its slope labelled at upper left. Note the significant increase in slope from shallow to deep sources. (c) Regression slopes plotted as a function of depth. Note the progressive transition from the shallow regime, where *h* should vary as $M_0^{1/3}$ to the deep one, where it becomes simply proportional to moment.

shown on Fig. 10, predict maximum amplitudes of 0.2 and 0.15 cm at Sites 21402 and 21419 (0.4 and 0.3 cm peak-to-peak), respectively, in good agreement with the amplitudes observed on the DART sensors (Fig. 1c), thus providing an order-of-magnitude quantitative verification of our interpretation of those two DART records.

3 NORMAL-MODE FORMALISM

We recall, following Ward (1980, 1981, 1982), that tsunamis can be considered a special branch of the Earth's spheroidal free oscillations, for a planetary structure including an ocean. While this approach cannot handle large-scale heterogeneity, such as the presence of continental masses, or large variations in bathymetry, it is extremely powerful for investigating the coupling of the ocean column with a solid substratum of finite rigidity, including realistic layered structures. The excitation of a tsunami by any dislocation source located in the solid Earth becomes a simple application of Gilbert's (1971) landmark formalism. Problems related to the duality between the classical and normal-mode formalism have been examined in previous papers (Okal 1982, 1988, 2003).[1]

---

[1] We correct a typographic error in eq. (27) of Okal (2003) which sould read

$$E^{\text{Tsunami}}_{\text{multiplet}} = \frac{1}{288\pi}\cdot\frac{\rho_w g}{\mu^2 a^2}\cdot l\cdot M_0^2 \qquad (27)$$

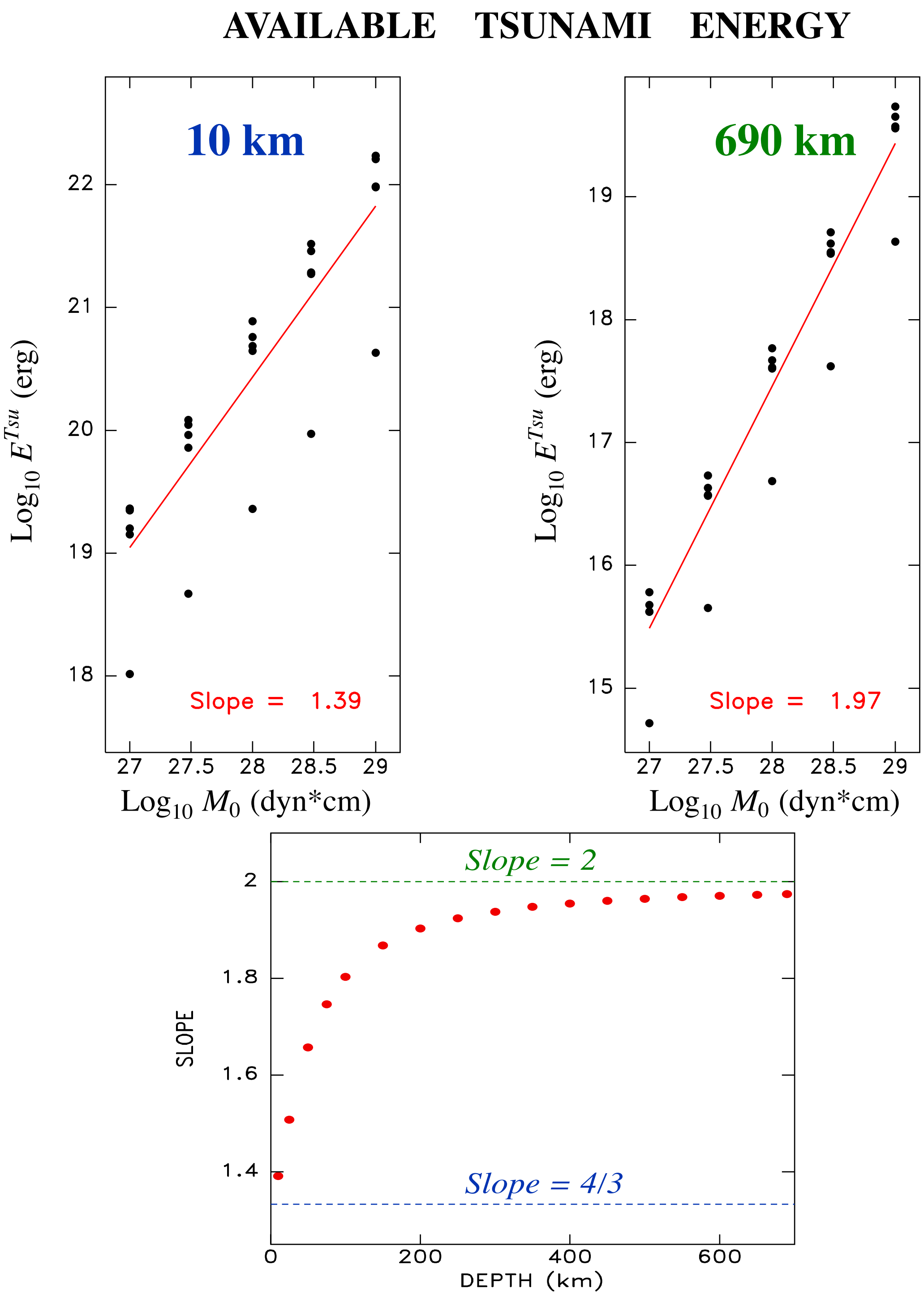

Figure 6. Top: available tsunami energy as a function of seismic moment, computed for a shallow source (left) and a deep one (right) by integrating the displacement fields (5) obtained from Mansinha & Smylie's (1971) algorithm. For each moment value, we use five different geometries, the strike-slip one being clearly deficient in energy. The red lines are power-law regressions of the data sets. Note that the shallow source features a slope close to the value 4/3 predicted by (3) and the deep one a slope matching the value 2 predicted by (6). Bottom: evolution of the regression slope as a function of depth, between values of 4/3 (shallow) and 2 (deep).

3.1 Tsunami energy in the normal-mode formalism

We will show here that under very simple assumptions, it is possible to reproduce eq. (6) in the normal-mode formalism. We start with eq. (49) of Okal (2003) which expresses the energy of a multiplet (with angular order l) excited by a source at depth z_s, which we rewrite in the slightly different notation used in the present paper:

$$E_{\text{Multip.}} = \frac{1}{36\pi}\,\frac{M_0^2}{\eta^2}\,\frac{\rho_w g}{r_s^2 \mu^2}\, l \left(A_3 e^{-\omega\gamma z_s} + B_3 e^{-\omega\delta z_s}\right)^2 \qquad (11)$$

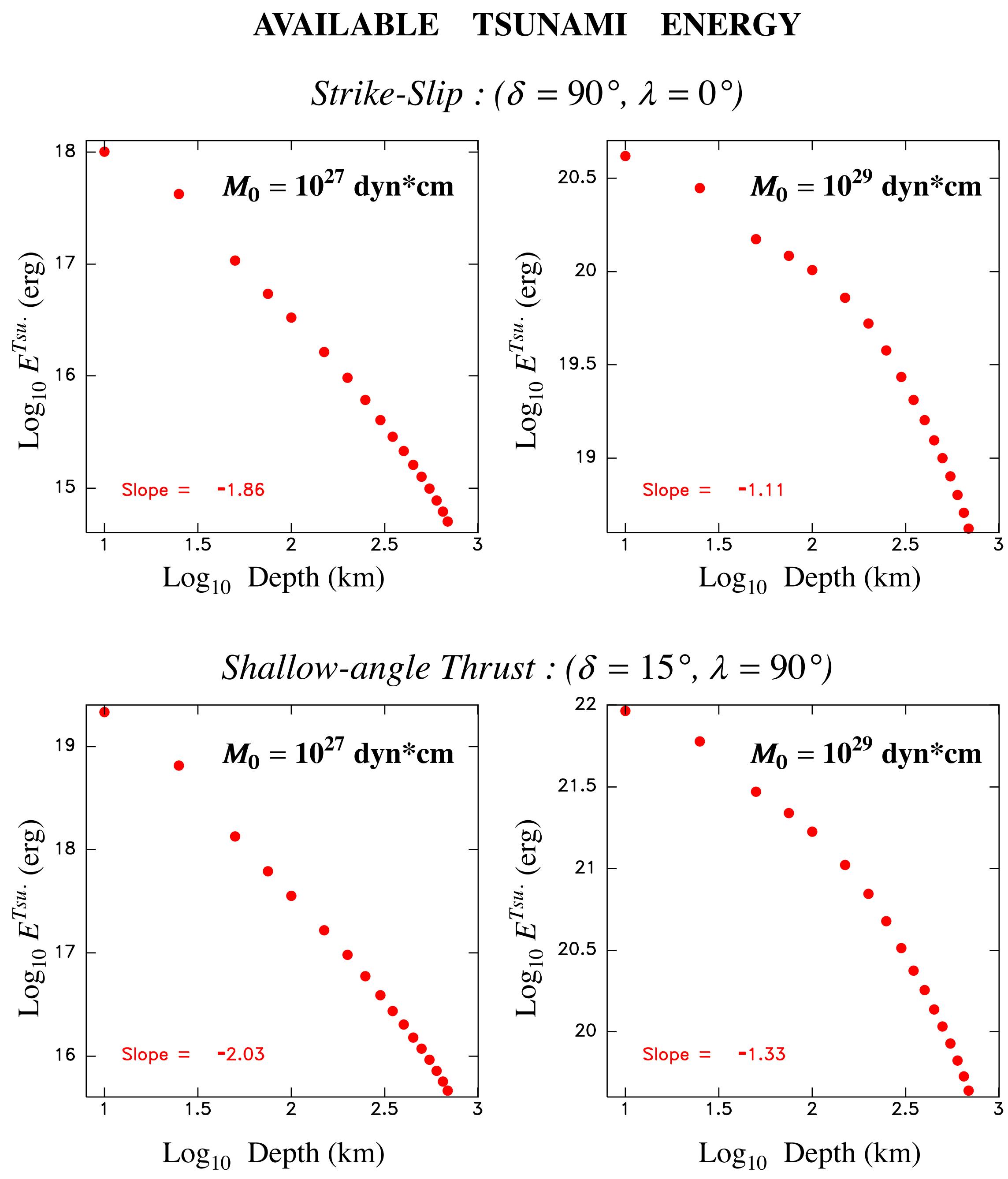

Figure 7. Available tsunami energy as a function of depth, for small (left) and large (right) seismic sources. Top: strike-slip mechanism; bottom: shallow angle thrust mechanism. Note that the small sources follow the z_s^{-2} power law, whereas the larger ones, for which source dimensions become comparable to z_s, depart from it, and feature curvature in the plot.

where η is the amplitude of vertical displacement at the surface of the ocean for the particular normalization of the multiplet considered, $r_s = a - z_s$ is the distance of the source to the centre of the Earth, γ and δ are the decay parameters of the P and S potentials of the pseudo-Rayleigh wave in the solid:

$$\gamma = \frac{\sqrt{1-\kappa^2/3}}{C}; \quad \delta = \frac{\sqrt{1-\kappa^2}}{C} \tag{12}$$

and A_3 and B_3 describe the expansion of the horizontal displacement of the eigenfunction in the solid Earth on the relevant exponentials:

$$u_x = l y_3 = \frac{\rho_w g}{\mu k}\left(A_3 e^{-\omega\gamma z} + B_3 e^{-\omega\delta z}\right) \tag{13}$$

Finally, $\kappa = C/\beta$ is the ratio of the tsunami phase velocity to the shear velocity of the solid ocean floor; it is always a small number, typically on the order of a few per cent. A_3 and B_3 are given by Okal (2003; eq. (47)) and are reproduced below:

$$A_3 = -\eta \times \frac{2-\kappa^2}{(2-\kappa^2)^2 - 4\sqrt{1-\kappa^2}\sqrt{1-\kappa^2/3}}$$

$$B_3 = \eta \times \frac{2\sqrt{1-\kappa^2}\sqrt{1-\kappa^2/3}}{(2-\kappa^2)^2 - 4\sqrt{1-\kappa^2}\sqrt{1-\kappa^2/3}} \tag{14}$$

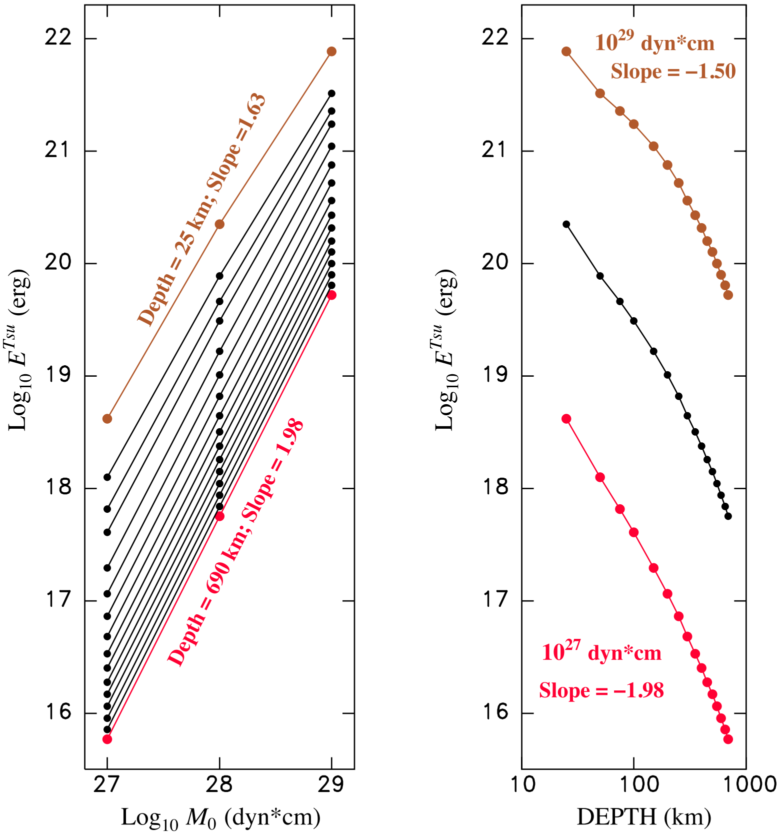

Figure 8. Logarithmic plots of the variation of tsunami energy computed from eq. (10) using MOST simulations for a 45°-thrust fault. Left: $E^{\mathrm{Tsu.}}$ versus M_0 at constant depth. Note excellent fit to the predicted M_0^2 dependence at great depths, but slower growth and curvature for shallower sources. Right: $E^{\mathrm{Tsu.}}$ versus source depth z_s at constant moment. Note excellent fit to the predicted z_s^{-2} dependence for small sources, but slower decay and curvature for larger ones.

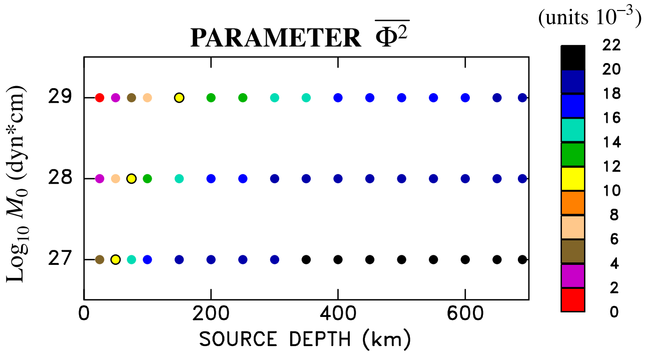

Figure 9. Estimates of the parameter $\overline{\Phi^2}$ obtained from the data set of tsunami energies in Fig. 8, by assuming compliance with eq. (6). For each combination of M_0 and z_s, the values of $\overline{\Phi^2}$ are colour-coded according to the palette bar at right. Note that in the range of compliance (small and/or deep earthquakes), $\overline{\Phi^2}$ stabilizes around 0.02, with significantly smaller values for large or shallow events for which source dimensions become comparable to z_s.

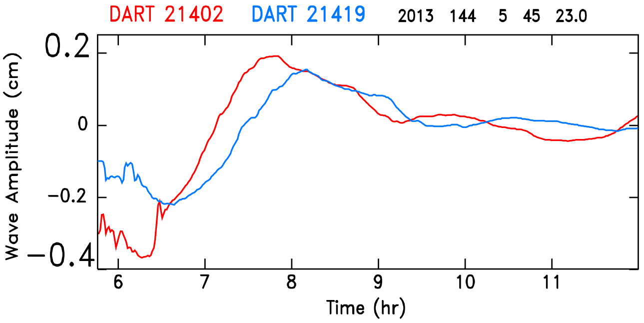

Figure 10. MOST simulation of the 2013 Sea of Okhotsk event, at the sites of DART sensors 21402 (in red) and 21419 (in blue). The time-series start at the origin time of the earthquake (05:45:23 GMT) and last until 12:00 GMT. Note the millimetric amplitudes and the low-frequency nature of the signals.

Eq. (11) was given in the case of a strike-slip source whose excitation coefficient K_2 can be expressed simply as a function of u_x, which itself has a simple dependence on depth. Other geometries would lead to comparable results. The total energy of the tsunami can be obtained by summing (over l) the contributions of all multiplets (11). This can be replaced by an integral over angular frequency ω:

$$E^{\mathrm{Tsu.}} = \frac{1}{36\pi}\,\frac{M_0^2}{\eta^2}\,\frac{\rho_w g}{r_s^2\mu^2}\,\frac{a}{U}\int_0^{\omega_c}\frac{a\omega}{C}\left(A_3 e^{-\omega\gamma z_s} + B_3 e^{-\omega\delta z_s}\right)^2 \mathrm{d}\omega \qquad (15)$$

where the integration should be stopped at the tsunami corner frequency ω_c of the source and a faster decaying spectrum used at higher frequencies (Okal 2003). However, for sources located 100 km or deeper into the Earth, and even for the largest earthquake moments, we find that the integral can be simply extended to infinity. Given

$$\int_0^\infty x \mathrm{e}^{-\tau x} \mathrm{d}x = \frac{1}{\tau^2} \tag{16}$$

we find that the integral in (15) takes the value

$$\frac{a}{C}\left[\frac{A_3^2}{4\gamma^2 z_\mathrm{s}^2} + \frac{B_3^2}{4\delta^2 z_\mathrm{s}^2} + \frac{2A_3 B_3}{(\gamma+\delta)^2 z_\mathrm{s}^2}\right]. \tag{17}$$

In the limit $\kappa \to 0$, both A_3 and B_3 are large, of order κ^{-2}, and the integral as written in (15) or (17) consists of subtracting two very large quantities to find their finite difference. A careful, third-order Taylor expansion of (17) shows that all terms of order κ^{-4} and κ^{-2} cancel out, and that (17) is simply of order 1 and can be approximated by $\frac{3}{64}\left(\frac{\eta^2 a C}{z_s^2}\right)$. There follows that

$$E^{\mathrm{Tsu.}} = F^{\mathrm{Modes}} \frac{M_0^2}{z_\mathrm{s}^2} \frac{\rho_\mathrm{w} g}{\mu^2} \frac{a^2}{r_\mathrm{s}^2} \frac{C}{U} \tag{18}$$

where F^{Modes} is a dimensionless parameter on the order of $\frac{1}{768\pi} \approx 1/2500$ for the strike-slip geometry considered here. Even for the deepest events ($z_\mathrm{s} = 690$ km), a/r_s remains of order 1, and so does the ratio of phase to group velocity, C/U, for the long wavelengths which we will see characterize tsunamis generated by deep sources. Eq. (18) then reduces to the form of (6), obtained in Section 2.2 under the classical formalism of the deformation of a homogeneous half-space. For other source geometries, the excitation coefficients (e.g. Kanamori & Cipar 1974) take a more complex form, but comparable results can be obtained: $E^{\mathrm{Tsu.}}$ should vary like M_0^2/z_s^2.

Another interesting parameter is the prominent frequency of the tsunami. It can be investigated by seeking the frequency ω_0 maximizing the spectral amplitude U_r in the far field. We focus once again on the simpler case of the strike-slip solution, for which the spectral amplitude can be obtained by combining eqs (7), (11) and (47) of Okal (2003). U_r is then proportional to

$$\omega^{1/2}\left[A_3 \exp\left(-\omega\gamma z_\mathrm{s}\right) + B_3 \exp\left(-\omega\delta z_\mathrm{s}\right)\right] \tag{19}$$

with γ, δ A_3, and B_3 given by (12) and (14). The maximum of (19) occurs when

$$\begin{aligned}&\frac{1}{2}\left[A_3 \exp\left(-\omega\gamma z_\mathrm{s}\right) + B_3 \exp\left(-\omega\delta z_\mathrm{s}\right)\right] \\ &\quad = \omega z_\mathrm{s}\left[\gamma A_3 \exp\left(-\omega\gamma z_\mathrm{s}\right) + \delta B_3 \exp\left(-\omega\delta z_\mathrm{s}\right)\right]\end{aligned} \tag{20}$$

which in the limit $\kappa \to 0$ has the solution

$$\frac{\omega_0 z_\mathrm{s}}{C} = 1 + \sqrt{3/4} \approx 1.87. \tag{21}$$

We thus predict that the prominent frequency of a deep tsunami should be inversely proportional to source depth z_s. We note that ω_0 is expected to depend on water depth H through the phase velocity C in (21), but the prominent wavelength Λ_0 does not. It is simply given by

$$\Lambda_0 \approx 3.4 z_\mathrm{s} \tag{22}$$

or about 2000 km for the source depth of the 2013 Sea of Okhotsk earthquake. Finally, we stress that these results are for point source double-couples and could be affected by source finiteness, especially for shallower sources.

It would also be interesting to predict the behaviour of the maximum amplitude $\eta_{\max}$ in the far field at any given point, as a function of source depth z_s (for a point source in the linear normal-mode theory, it is always expected to scale directly with M_0), but this is made difficult by the fact that, in the normal-mode approach, it will result from a summation over l (or from an integration over ω of its Fourier transform), and its dependence on depth cannot be simply predicted.

3.2 Normal-mode synthetics

Normal-mode synthetics were computed for a variety of depths and focal geometries. Because the above theory relates to a point-source double-couple, a single value of the moment was used, namely $M_0 = 10^{27}$ dyn cm, the smallest source size used in Section 2. Eleven centroid depths were used, ranging from 25 km to 690 km. For each of the five focal mechanism geometries, a single time-series was computed at an angular distance $\theta = 90^\circ$ and in the lobe of focal mechanism radiation (e.g. at an azimuth of 45° from the fault strike in the case of the strike-slip mechanisms). Finally, three different ocean depths (2 km, 4 km, 5 km) were considered, for a total of 165 synthetics.

For each water depth, tsunami normal modes were computed at ~70 representative frequencies, ranging from 0.09 to 4 mHz. Synthetic maregrams were then built in the frequency domain, by systematic interpolation between those frequencies (Kanamori & Stewart 1976). We recall that normal-mode theory, while unable to describe non-linear effects, automatically handles dispersive aspects of tsunami propagation outside the shallow-water approximation.

Once a time-series $\eta(t)$ is obtained at a virtual gauge located at an angular distance θ from the source, the energy of the tsunami can be computed by integrating over time the energy flux through a wave front sweeping the oceanic column. By virtue of Parseval's theorem, this integration can be carried out in the frequency domain, where the contribution of vertical motion to the spectrum of kinetic energy density at the surface can be written as

$$e_z(\omega) = \frac{1}{2}\rho_\mathrm{w}\left[\omega\bar{\eta}(\omega)\right]^2 \tag{23}$$

where $\bar{\eta}(\omega)$ is the Fourier transform of $\eta(t)$; $e_z(\omega)$ is a Fourier-domain counterpart to $E_z(t)$ in eq. (7). For a general angular frequency ω, which may not satisfy the shallow-water approximation, and at depth z inside the water column ($z > 0$), the spectral amplitude of vertical displacement will be $\bar{\eta}(\omega)$ multiplied by ($\sinh k(H - z) / \sinh kH$), where k is the wavenumber related to ω through the classical dispersion relation

$$\omega^2 = gk \cdot \tanh(kH). \tag{24}$$

Meanwhile, the horizontal velocity spectral amplitude will be

$$v_x(\omega) = \omega\bar{\eta}(\omega)\frac{\cosh k(H-z)}{\sinh kH} \tag{25}$$

so that the total kinetic energy density at depth z will be

$$e(z) = e_x + e_z = \frac{1}{2}\rho_\mathrm{w}\omega^2\bar{\eta}(\omega)^2\frac{\cosh 2k(H-z)}{\sinh^2 kH} \tag{26}$$

and the kinetic energy flux integrated through the entire ocean column

$$F_K(\omega) = U(\omega)\int_0^H e(z)\,\mathrm{d}z = \frac{1}{4}\rho_\mathrm{w}\frac{U(\omega)}{k(\omega)}\omega^2\bar{\eta}(\omega)^2\frac{\sinh 2kH}{\sinh^2 kH} \tag{27}$$

where $U(\omega)$ is the group velocity of the wave. To obtain the total energy of the tsunami, there remains to add the equal contribution of gravitational energy, to integrate (27) over ω (under Parseval's theorem), and to integrate the result along a horizontal arc

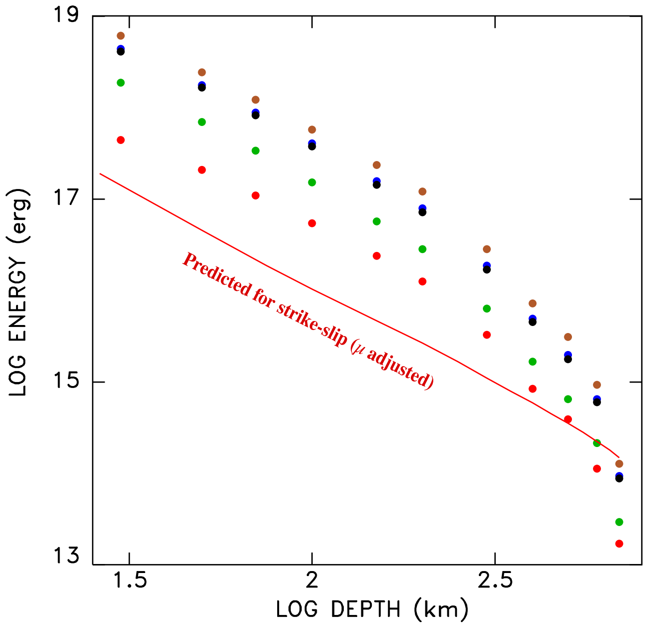

Figure 11. Energy as a function of depth from normal-mode synthetics. Individual estimates obtained by integration of the times-series at the virtual gauges considered for each of the five focal geometries are colour-coded as in Fig. 5. See the text for details. The red line is the power law predicted by eq. (6), adjusted at each source depth for the variable value of the average rigidity μ above the source.

perpendicular to the propagation (the equator of the source for a distance $\theta = 90^\circ$), yielding

$$E^{\mathrm{Tsu.}} = \int_0^{2\pi} a\, \mathrm{d}\phi \frac{1}{\pi} \int_{-\infty}^{+\infty} R^2(\phi;\omega)\, F_K(\omega)\, \mathrm{d}\omega \tag{28}$$

where a is the Earth's radius, and R a radiation pattern coefficient (relative to that at the virtual gauge), which could depend on ω for complex mechanisms. In the case of a strike-slip mechanism, $R = \sin 2\phi$ and the average of R^2 would just be 1/2, leading in this particular case to

$$E^{\mathrm{Tsu.}} = 2a \int_0^{\infty} F_K(\omega)\, \mathrm{d}\omega. \tag{29}$$

The energy computed in (29) would be expected to be equivalent to (6). This is verified on Fig. 11 which offers an acceptable fit to (6) between depths of 150 and 690 km.

We also present in Fig. 12 the dominant frequency ω_0 (defined as that featuring a maximum in the spectral amplitude $\bar{\eta}(\omega)$ of the normal-mode synthetics) for water depths $H = 4$ km (a) and 2 km (b). We note that for $z_s \leq 350$ km, ω_0 follows its value predicted by eq. (21) (dashed lines on the plots), but that it remains somewhat larger at greater depths. We presently do not have a simple interpretation of this behaviour. Note that other source geometries generally result in lower prominent frequencies, and a possibly weaker dependence of ω_0 on depth, due to the complexity of the eigenfunction components governing their excitation. Fig. 12(c) combines the results of frames (a) and (b), and expresses them as a function of the dominant wavelength Λ_0. As expected from eq. (22), this eliminates the dependence on water depth H, but the same misfit occurs at the greatest depths.

3.3 Normal-mode simulation of the deep Okhotsk Sea tsunami

Finally, we apply here the normal-mode approach to the modelling of the records at DART Stations 21402 and 21419 (Fig. 1). We consider a point-source double-couple with the Global-CMT focal solution ($\phi = 189^\circ$; $\delta = 11^\circ$; $\lambda = -93^\circ$), and the simplified (if not outright simplistic) model of a homogeneous ocean of depth 4 km. Our synthetics are computed using the same algorithm as in Section 3.2, but for the correct station geometry ($\theta = 8.67^\circ$, $\phi_s = 159^\circ$ for 21402; $\theta = 10.36^\circ$, $\phi_s = 172^\circ$ for 21419). As shown on Fig. 13, and despite the shortcomings of this approach (the uniform bathymetry and the point source), the order of magnitude of the amplitude of the tsunami at the two DART gauges (a few millimetres peak-to-peak; see Fig. 1c) is correctly predicted, this result being essentially independent of the water depth H selected for the model.

4 DISCUSSION AND CONCLUSION

The present study has established theoretical bases for the variation of tsunami energy as a function of seismic moment M_0 and source depth z_s. Despite the exponential form of the decay of the various components of the eigenfunction with depth, we find that tsunami energy is expected to decay as z_s^{-2} reflecting integration of excitation over frequency. This result is valid as long as source depth remains greater that source dimensions, and was verified by three different means: the calculation of the available tsunami energy in the formalism of Mansinha & Smylie (1971), the integration of tsunami energy along a wave front of virtual gauges simulated numerically using the MOST code, and finally, the estimate of energy flux at virtual gauges using the formalism of normal-mode summation.

It remains an unescapable fact that tsunamis generated by deep earthquakes are of moderate energy, and do not feature appreciable risk, at least as presently documented. On Fig. 14, we use eq. (29) to estimate the available tsunami energy $E^{\mathrm{Tsu.}}$ for all large earthquakes with centroids deeper than 100 km, for the duration of the Global-CMT catalogue (1977–2015). The maximum in $E^{\mathrm{Tsu.}}$, on the order of 10^{18} erg, is shared by the 2013 Okhostk deep earthquake (O13 on Fig. 14) and the smaller and much shallower Aleutian event of 2014 June 23 (A14; $z_s = 104$ km; $M_0 = 1.0 \times 10^{28}$ dyn cm), the energy ratio between the two events being predicted at $(6/4)^2 = 2.25$; we have verified that a tsunami was indeed recorded from the 2014 Aleutian event on DART sensor 21414, at an epicentral distance of 340 km, with a peak-to-peak amplitude of 6 mm or 1.5 times its counterpart at DART Buoy 21402 in 2013 (or a factor of precisely 9/4 in energy); despite the large disparity in depth, this excellent agreement may be due to a common tectonic environment (epicentre in a back-arc basin) and comparable focal mechanism.

By contrast, the megathrust events of 2004 in Sumatra and 2011 in Tohoku ($M_0 = 1.2 \times 10^{30}$ and 5.3×10^{29} dyn cm, respectively) had tsunami energies of 10^{24} and 3×10^{23} erg, respectively, estimated from the $M_0^{4/3}$ scaling appropriate for shallow events (Okal 2003, eq. 57); the 1960 Chilean earthquake, the largest ever recorded may have reached $E^{\mathrm{Tsu.}} = 5 \times 10^{24}$ erg. Note that these numbers represent only estimates from simple models using a laterally homogeneous Earth structure, but the five-to-six orders of magnitude difference between the shallow and deep energy maxima would convert to 2.5–3 orders of magnitude in wave amplitude, a ratio reasonably representative of observed amplitudes (a few mm in the regional field for Okhotsk, versus 5 m for Tohoku, as measured at the regional TM1 deep sea sensor (Fujii *et al.* 2011)).

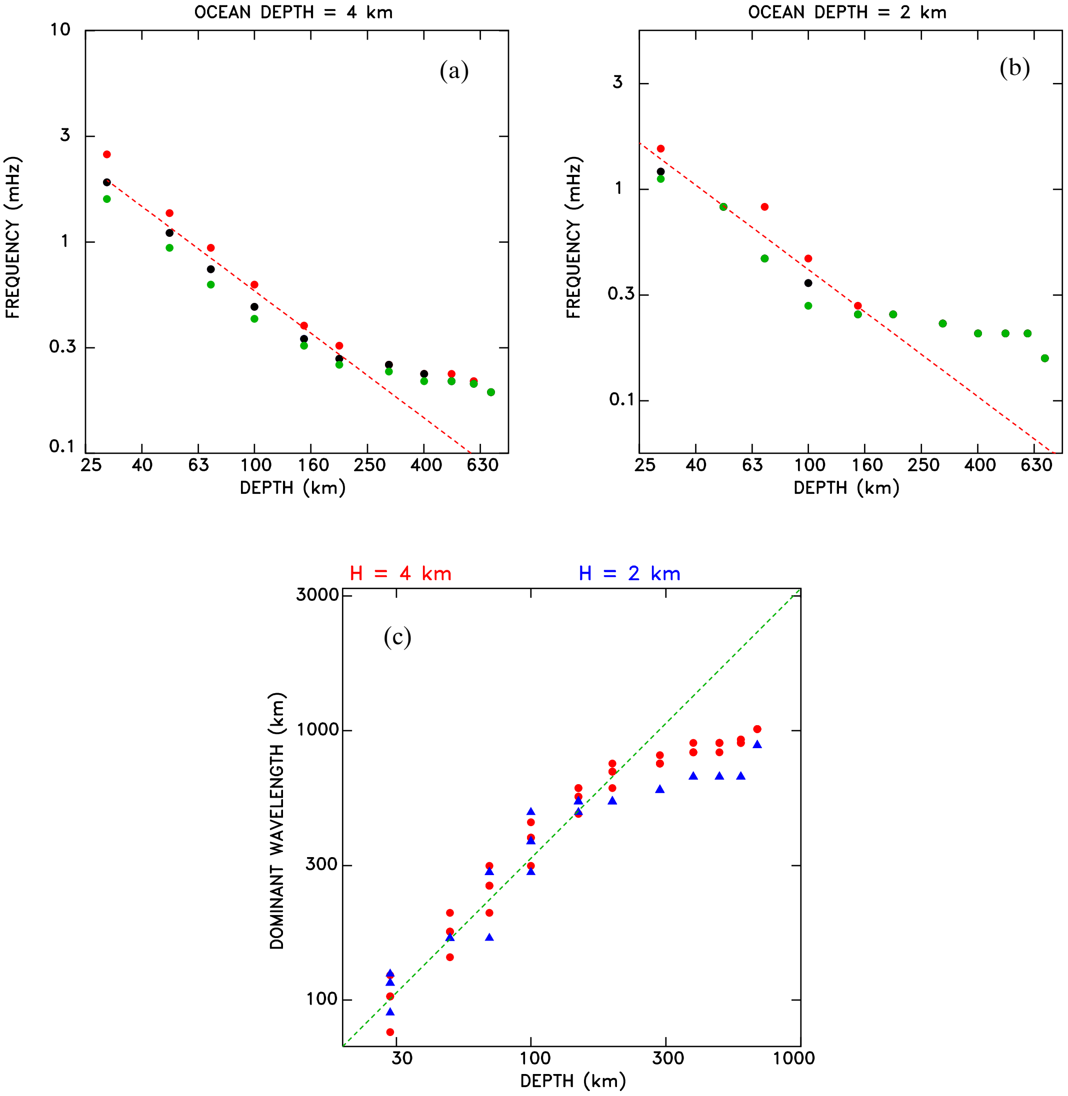

Figure 12. Dominant frequency as a function of depth from normal-mode synthetics for water depths of 4 km (a) and 2 km (b). The frequency carrying maximum spectral amplitude for each of the times-series at the virtual gauges is colour-coded for focal mechanism as in Fig. 11. The dashed line is the theoretically predicted power law (21). (c) Dominant wavelengths as a function of depth. This plot regroups all data for $H = 4$ km (red circles) and $H = 2$ km (blue triangles). Note that Λ_0 is independent of H. The dashed line is the theoretical line (22).

The distribution on Fig. 14, featuring a low in estimated tsunami energy between 200 and 550 km, expresses principally the classical distribution of seismic moment release as a function of depth (e.g. Frohlich 2006). In this context, it is extremely improbable that intermediate earthquakes with centroid depths in the 200–550 km range would ever produce observable tsunamis.

As for the deepest earthquakes with potential to excite detectable tsunamis, they are represented on Fig. 14 by two events: the 2013 Sea of Okhotsk and 1994 Bolivian shocks (O13 and B94, respectively). In this context, one cannot help but notice that, over the past 60 yr, the maximum size of any documented deep earthquake has risen regularly, if very slowly, by a full order of magnitude in seismic moment. As sketched on Fig. 15, the largest event known in the late 1960s was the Peru–Brazil earthquake of 1963 August 15 (PB on Fig. 15), whose moment was later given by Gilbert & Dziewonski (1975) as 3.9×10^{27} dyn cm, although later work on the deep Spanish earthquake of 1954 March 29 (S) and the Peru–Colombia event of 1922 January 17 (PC) yielded larger values (7×10^{27} and 9.4×10^{27} dyn cm, respectively) (Chung & Kanamori 1976; Huang *et al.* 1998). The Colombian deep shock of 1970 July 31 (C; 1.8×10^{28} dyn cm) (Gilbert & Dziewonski 1975) raised the bar significantly, and it was perceived for two decades as a probable natural limit for deep events at the bottom of Wadati-Benioff zones. The occurrence, after 24 yr, of the Bolivian shock of 1994 June 9 (B; 2.6×10^{28} dyn cm) (Dziewonski *et al.* 1995), and again, after 19 more years, of the Sea of Okhotsk earthquake of 2013 May 24 (O), keeps *de facto* resetting upwards the size of the maximum deep earthquake, and it becomes legitimate to speculate what a data-based consensus in this respect may look like in the year 2040 or 2060, the question of how to possibly extrapolate Fig. 15 in the future remaining wide-open.

In the context of the widely proposed model of deep seismogenesis being nucleated by transformational faulting in a zone of metastable olivine inside the subducting plate (e.g. Kirby *et al.* 1996), an argument has often been made that such domains were too narrow to accommodate events of the size of the 1994 Bolivian earthquake (Wiens *et al.* 1994; Ye *et al.* 2013). However, Green *et al.* (1992) have documented in laboratory experiments the case

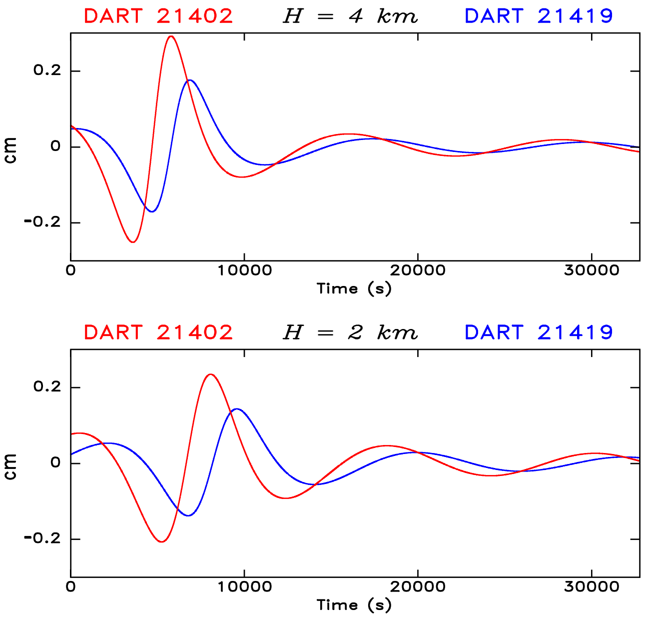

Figure 13. Normal-mode simulations of the 2013 Sea of Okhotsk DART records for sensors 21402 (red) and 21419 (blue). The top frame uses an ocean of homogeneous depth $H = 4$ km, the bottom one a shallower structure ($H = 2$ km), more representative of the Sea of Okhotsk. Note that in all cases, peak-to-peak amplitudes on the order of 3–5 mm are predicted, in agreement with the observed values (Fig. 1).

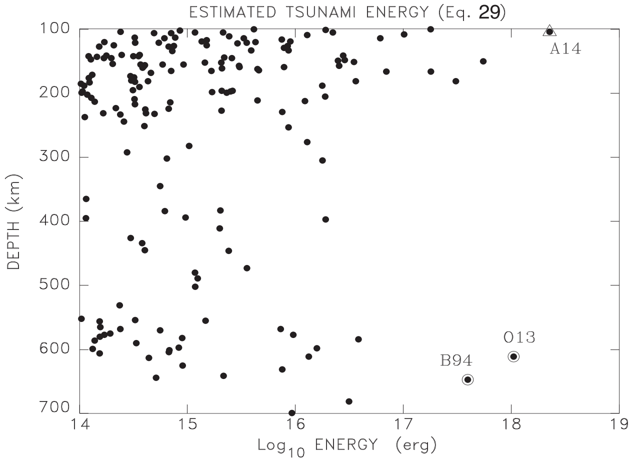

Figure 14. Estimated tsunami energy computed from eq. (29) for Global-CMT solutions with centroidal depths $z_s \geq 100$ km. Highlighted are the 2013 Sea of Okhotsk (O13) and 1994 Bolivia (B94) deep shocks, as well as the intermediate-depth 2014 Aleutian event (A14). Note low tsunamigenic potential in the 200–550 km depth range.

of a crack generated by transformational faulting extending outside the particular crystal involved in the transformation, which largely removes the objection to the nucleation of large deep events, which at any rate are indeed observed. Therefore, and given the significant along-trench dimension of most subduction systems, it is not unreasonable to suggest the potential occurrence of deep earthquakes of a size even greater than in 2013. Under such speculative conditions, a near-field deep-water tsunami amplitude of few cm may be envisioned which could conceivably be amplified to decimetric levels in bays and harbours, at which level slight damage could not be ruled out. Furthermore, we note that the 2013 earthquake was reported felt at a Modified Mercalli Intensity (MMI) of V in Petropavlovsk, and one can thus speculate that a larger earthquake might reach MMI = VI, with the potential for destabilization of precarious underwater sedimentary structures, and thus for triggering of tsunamigenic landslides.

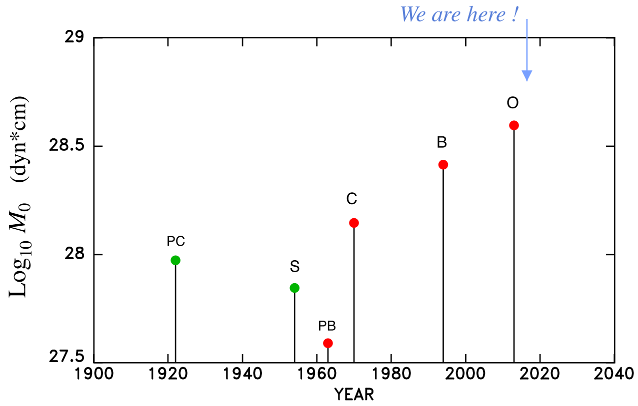

Figure 15. Maximum moment known for deep earthquakes as a function of time. The two events predating 1960 are shown in green since their moments were determined after later and larger events were already documented. See the text for details.

In conclusion, and despite the clearly speculative nature of the extrapolations in seismic moment presented in the above discussion, we believe that the possibility that tsunamis generated by deep earthquakes might reach amplitudes of a possibly damaging, if certainly not catastrophic, nature should not be dismissed *a priori* when assessing regional tsunami risk in the vicinity of subduction zones.

ACKNOWLEDGEMENTS

We thank Andreĭ Zaĭtsev and Yefim Pelinovskiĭ for an advanced copy of their paper, and Fred Pollitz for a customized computation of static displacements in a realistic spherical Earth. Maps were drawn using the GMT software (Wessel & Smith 1991). The paper was improved by the comments of two anonymous reviewers.

REFERENCES

Aida, L., 1977. Simulations of large tsunamis occurring in the past off the coast of the Sanriku district, *Bull. Earthq. Res. Inst. Univ. Tokyo,* **52,** 71–101 [in Japanese].

Aki, K. & Richards, P.G., 1980. *Quantitative Seismology,* W.H. Freeman, 932 pp.

Bernard, E.N., González, F.I., Meining, C. & Milburn, H.B., 2001. Early detection and real-time reporting of deep-ocean tsunamis, in *Proc. Int. Tsunami Symp.,* 7–10 August 2001, pp. 97–108, Seattle.

Chung, W.-Y. & Kanamori, H., 1976. Source process and tectonic implications of the Spanish deep-focus earthquake of March 29, 1954, *Phys. Earth planet. Inter.,* **13,** 85–96.

Dziewonski, A.M., Ekström, G. & Salganik, M.P., 1995. Centroid-moment tensor solutions for April–June 1994, *Phys. Earth planet. Inter.,* **88,** 69–78.

Ewing, W.M., Jardetzky, W.S. & Press, F., 1957. *Elastic Waves in Layered Media,* McGraw-Hill, 380 pp.

Frohlich, C., 2006. *Deep Earthquakes,* Cambridge Univ. Press, 566 pp.

Fujii, Y., Satake, K., Sakai, S., Shinohara, M. & Kanazawa, T., 2011. Tsunami source of the off the Pacific coast of Tohoku earthquake, *Earth Plan. Space,* **63,** 815–820.

Geller, R.J., 1976. Scaling relations for earthquake source parameters and magnitudes, *Bull. seism. Soc. Am.,* **66,** 1501–1523.

Gilbert, J.F., 1971. Excitation of the normal modes of the Earth by earthquake sources, *Geophys. J. R. astr. Soc.,* **22,** 223–226.

Gilbert, J.F. & Dziewonski, A.M., 1975. An application of normal mode theory to the retrieval of structural parameters and source mechanisms from seismic spectra, *Phil. Trans. R. Soc. A,* **278,** 187–269.

Godunov, S.K., 1959. Finite difference methods for numerical computations of discontinuous solutions of the equations of fluid dynamics, *Mat. Sb.,* **47,** 271–295.

Green, H.W., II, Scholz, C.H., Tingle, T.N., Young, T.E. & Koczynski, T.A., 1992. Acoustic emissions produced by anticrack faulting during the olivine → spinel transformation, *Geophys. Res. Lett.,* **19,** 789–792.

Huang, W.-C., Okal, E.A., Ekström, G. & Salganik, M.P., 1998. Centroid moment tensor solutions for deep earthquakes predating the digital era: the historical dataset (1907–1961), *Phys. Earth planet. Inter.,* **106,** 181–190.

Kajiura, K., 1981. Tsunami energy in relation to parameters of the earthquake fault model, *Bull. Earthq. Res. Inst. Univ. Tokyo,* **56,** 415–440.

Kanamori, H. & Anderson, D.L., 1975. Theoretical basis of some empirical relations in seismology, *Bull. seism. Soc. Am.,* **65,** 1073–1095.

Kanamori, H. & Cipar, J.J., 1974. Focal process of the great Chilean earthquake, May 22, 1960, *Phys. Earth planet. Inter.,* **9,** 128–136.

Kanamori, H. & Stewart, G.S., 1976. Mode of the strain release along the Gibbs Fracture Zone, Mid-Atlantic ridge, *Phys. Earth planet. Inter.,* **11,** 312–332.

Kirby, S.H., Stein, S., Okal, E.A. & Rubie, D., 1996. Deep earthquakes and metastable mantle phase transformations in subducting oceanic lithosphere, *Rev. Geophys. Space Phys.,* **34,** 261–306.

Levin, B.V. & Nosov, M.A., 2005. *Fizika Tsunami,* Yanus-K [in Russian].

Mansinha, L. & Smylie, D.E., 1971. The displacement fields of inclined faults, *Bull. seism. Soc. Am.,* **61,** 1433–1440.

Mofjeld, H.O., 2008. Tsunami measurements, in *The Sea: Ideas and Observations on Progress in the Study of the Seas,* Vol. 15, pp. 201–235, eds Bernard, E.N. & Robinson, A.R., Harvard Univ. Press.

Okada, Y., 1985. Surface deformation due to shear and tensile faults in a half-space, *Bull. seism. Soc. Am.,* **75,** 1134–1154.

Okada, Y., 1995. Simulated empirical law of coseismic crustal deformation, *J. Phys. Earth,* **43,** 697–713.

Okal, E.A., 1982. Mode-wave equivalence and other asymptotic problems in tsunami theory, *Phys. Earth planet. Inter.,* **30,** 1–11.

Okal, E.A., 1988. Seismic parameters controlling far-field tsunami amplitudes: a review, *Nat. Hazards,* **1,** 67–96.

Okal, E.A., 1989. A theoretical discussion of time-domain magnitudes: the Prague formula for M_s and the mantle magnitude M_m, *J. geophys. Res.,* **94,** 4194–4204.

Okal, E.A., 1990. M_m: a variable-period mantle magnitude for intermediate and deep earthquakes, *Pure appl. Geophys.,* **134,** 333–354.

Okal, E.A., 1992. A student's guide to teleseismic body-wave amplitudes, *Seismol. Res. Lett.,* **63,** 169–180.

Okal, E.A., 2003. Normal modes energetics for far-field tsunamis generated by dislocations and landslides, *Pure appl. Geophys.,* **160,** 2189–2221.

Okal, E.A., 2014. Un tsunami engendré par le séisme profond ($h = 603$ km) de la Mer d'Okhotsk du 24 mai 2013: Est-ce une idée outrancière?, in *Actes Sémin. Ann. Hydroacoust. Tsunamis,* Commissariat à l'Energie Atomique, Paris [abstract].

Okal, E.A. & Bina, C.R., 1998. On the cessation of seismicity at the base of the transition zone, *J. Seismol.,* **2,** 65–86.

Pollitz, F.F., 1996. Coseismic deformation from earthquake faulting on a layered spherical Earth, *Geophys. J. Int.,* **125,** 1–14.

Schwartz, S.Y. & Rokosky, J.M., 2007. Slow slip events and seismic tremor at Circum-Pacific subduction zones, *Rev. Geophys.,* **45,** RG3004, doi:10.1029/2006RG000208.

Synolakis, C.E., 2003. Tsunami and seiche, in *Earthquake Engineering Handbook,* eds Chen, W.-F. & Scawthron, C., pp. 9_1–9_90, CRC Press.

Titov, V.V. & Synolakis, C.E., 1998. Numerical modeling of tidal wave runup, *J. Waterway, Port Coastal Ocean Eng.,* **B124,** 157–171.

Titov, V.V., Kânoǧlu, U. & Synolakis, C.E., 2016. Development of MOST for real-time tsunami forecasting, *J. Waterway, Port, Coastal, Ocean Eng.,* **142**(6), 03116004, doi:10.1061/(ASCE)WW.1943-5460.0000357.

Ward, S.N., 1980. Relationships of tsunami generation and an earthquake source, *J. Phys. Earth,* **28,** 441–474.

Ward, S.N., 1981. On tsunami nucleation: I. A point source, *J. geophys. Res.,* **86,** 7895–7900.

Ward, S.N., 1982. On tsunami nucleation: II. An instantaneous modulated line source, *Phys. Earth planet. Inter.,* **27,** 273–285.

Wessel, P. & Smith, W.H.F., 1991. Free software helps map and display data, *EOS, Trans. Am. geophys. Un.,* **72,** 441 and 445–446.

Wiens, D.A., McGuire, J.J., Shore, P.G., Bevis, M.G., Draunidalo, K., Prasad, G. & Helu, S.P., 1994. A deep earthquake aftershock sequence and implications for the rupture mechanism of deep earthquakes, *Nature,* **372,** 540–543.

Williamson, A., Newman, A.V. & Okal, E.A., 2015. Detection and modeling of the tsunami generated by 2013 Okhotsk deep focus earthquake, *EOS, Trans. Am. geophys. Un.,* **96**(53), NH23A–1863 [abstract].

Ye, L., Lay, T., Kanamori, H. & Koper, K.D., 2013. Energy release of the 2013 $M_w = 8.3$ Sea of Okhotsk earthquake and deep slab stress heterogeneity, *Science,* **341,** 1380–1384.

Zaitsev, A.I., Pelinovsky, E.N., Kurkin, A.A., Kostenko, I.S. & Yalçıner, A., 2016. The possibility of tsunami in the Sea of Okhotsk caused by deep-focus earthquakes, *Izv. Atmos. Ocean. Phys.,* **52,** 217–224.

APPENDIX: ESTIMATING A SEISMIC MOMENT FROM DART RECORDS OF THE 2013 SEA OF OKHOTSK EARTHQUAKE

We attempt here a quantification of the main signals on Fig. 1, by assuming that they represent mantle surface waves; body waves would have energy concentrated at much higher frequencies which cannot be recorded reliably with a sampling of 1 min.

The classical theory of Rayleigh waves propagating in a half-space overlain by a fluid layer of thickness H (Ewing *et al*. 1957) predicts an impedance (ratio of pressure p to vertical displacement u_z) at the interface

$$Z = \frac{p}{u_z} = \omega \rho_w \alpha_w \tan(k_z H) \qquad \text{(A1)}$$

where ω is angular frequency, ρ_w the density of seawater, and α_w its acoustic (P) wave velocity. For a long-period Rayleigh wave, the phase velocity (typically 5 km s^{-1}) is much greater than α_w (1.5 km s^{-1}), so that the vertical wave number k_z in the oceanic column is real and can be approximated by (ω/α_w). If p is then expressed as an equivalent incremental height η of the sea surface, one obtains

$$\frac{u_z}{\eta} = \frac{g}{\omega \alpha_w \tan\left(\frac{\omega H}{\alpha_w}\right)} \underset{\omega \to 0}{\approx} \frac{g}{\omega^2 H} \qquad \text{(A2)}$$

meaning, incidentally, that the pressure sensor functions as an accelerometer (it would respond to velocity in the case of body waves). For a period $T \approx 100$ s, and $H = 5$ km, this ratio is about 0.5, and the zero-to-peak equivalent amplitude $\eta = 1.5$ cm apparent on Fig. 1 translates into a vertical ground motion of ~0.7 cm at the seafloor location of the sensor. In turn, following Okal (1989; eq. (21)), one can infer a Rayleigh wave spectral amplitude on the order of 23 cm s. Applying the M_m algorithm for deep earthquakes (Okal 1990), at a distance of 5°, one infers $M_m = 8.7$ or $M_0 = 5 \times 10^{28}$ dyn cm. Because of the large number of approximations involved in this computation, notably due to the undersampling of the time-series and the short epicentral distance over which the validity of M_m for deep sources has not been tested, the excellent agreement with the published moment (4×10^{28} dyn cm) should not be taken as more than an order-of-magnitude verification that the main signals in the DART records can be reasonably identified as the passage of mantle waves, without the need to invoke the complex formalism of coupling of tsunami waves to acoustic oscillations of the water column (Levin & Nosov 2005; Zaitsev *et al*. 2016).